nature communications

Article

https://doi.org/10.1038/s41467-026-73933-0

ARID1A loss drives gastric signet ring cell carcinoma by regulating mucin production and secretion

Received: 20 October 2024

Accepted: 23 May 2026

Published online: 02 June 2026

Check for updates

Hongyu Liu[1,9], Ailing Zhong[1,9], Zhenghao Lu[2,3,9], Limin Gao[4,9], Mengsha Zhang[1], Jiaxin Li[1], Yingjie Wang[1], Yiyun Wang[1], Lanxin Zhang[1], Jiabo Zhang[1], Xiangyu Pan[1], Xuelan Chen[1], Jingyao Chen[1], Siyu He[1], Xinyuan Wang[1], Xudong Wan[1], Xintong Deng[1], Tingfa Peng[5], Jian Wang[1], Jiajia Du[1], Kun Yang[2], Kai Liu[2], Xinzu Chen[2], Xiaolong Chen[2], Zhe Feng[6], Baohong Wu[1], Jing Xu[1], Linyong Zhao[2], Weihan Zhang[2], Shengyong Yang[1], Yuan Wang[1], Lu Chen[1], Zhihong Xue[1], Chengjian Zhao[1], Lunzhi Dai[1], Feifei Na[7] ✉, Jiankun Hu[2] ✉, Yu Liu[1] ✉ & Chong Chen[1,8] ✉

Signet ring cell carcinoma (SRCC) is a lethal malignancy with distinct histologic features, characterized by accumulated mucins in the cytoplasm which compress nuclei. Gastric SRCC is the most common SRCC whose incidence is increasing in recent years. The molecular mechanisms underlying the histopathology remain poorly understood. Here, we report that AT-rich interactive domain-containing protein 1 A (ARID1A), one of the most frequently mutated genes in gastric SRCC, functions as a bona fide tumor suppressor. Its loss, together with *Trp53* and *Pten* loss, drives SRCC in mice. Mechanistically, *Arid1a* loss upregulates the expressions of mucins through the competing BRD9-containing ncBAF complex. And mucin secretion is impaired by the downregulation of *Scin*, a direct target of *Arid1a* in SRCC. Inhibition of *Brd9* ameliorates the malignancy of SRCC. Thus, our study reveals dual roles of *ARID1A* in both mucin production and secretion, providing new mechanistic insights and potential therapeutic vulnerabilities in SRCC.

Signet ring cell carcinoma (SRCC) is a histologically distinct form of highly malignant adenocarcinoma, characterized by a large vacuole and the resulting cell periphery-localized nucleus, resembling a signet ring[1,2]. The most common SRCC tumors occur in the stomach, and less frequently in colorectum and other sites[3–5]. Gastric SRCC accounts for approximately 10% of all gastric cancers, with an increasing incidence in recent years, and is associated with poor prognosis[6–9]. It is believed that this special histologic appearance is due to large amounts of mucins produced by SRCC cells and their deficient ability to export them[10–15]. However, the molecular mechanisms underlying these malignancy-associated abnormalities remain poorly understood.

[1]State Key Laboratory of Biotherapy and Cancer Center and National Clinical Research Center for Geriatrics, West China Hospital, Sichuan University, Chengdu, Sichuan, China. [2]Department of Gastrointestinal Surgery and Laboratory of Gastric Cancer, State Key Laboratory of Biotherapy, West China Hospital, Sichuan University, Chengdu, Sichuan, China. [3]Chengdu OrganoidMed Medical Laboratory, West China Health Valley, Chengdu, Sichuan, China. [4]Department of Pathology, West China Hospital, Sichuan University, Chengdu, Sichuan, China. [5]Department of Gastroenterology, Armed Police Forces Hospital of Sichuan, Chengdu, Sichuan, China. [6]Department of Gastroenterology, West China Hospital, Sichuan University, Chengdu, Sichuan, China. [7]Division of Thoracic Tumor Multimodality Treatment, Cancer Center, West China Hospital, Sichuan University, Chengdu, Sichuan, China. [8]Frontiers Medical Center, Tianfu Jincheng Laboratory, Chengdu, Sichuan, China. [9]These authors contributed equally: Hongyu Liu, Ailing Zhong, Zhenghao Lu, Limin Gao. ✉e-mail: nafeifei@foxmail.com; hujkwch@126.com; yuliuscu@scu.edu.cn; chongchen@scu.edu.cn

Recent progress in cancer genomics have identified a spectrum of genomic alterations in SRCC[9,16,17]. In addition to *TP53*, the most frequently mutated gene in both SRCC and non-SRCC tumors, *ARID1A* and *CDH1* exhibit particularly high mutation rates in SRCC. Other alterations, such as *CLDN18-ARHGAP26/6* fusions, are also detected in approximately 20% of SRCC patients[9,18,19]. *CDH1* encodes the cell-cell adhesion molecule E-cadherin, and its heterozygous loss significantly promotes SRCC formation in mice treated with N-methyl-N-nitrosourea (MNU), whereas it has a limited effect on tubular adenoma development[20]. Similarly, *CDH1* knockout in human gastric organoids induces morphological changes similar to SRCC[21–24]. It has also been suggested that downregulation of Wnt signaling facilitates the SRCC morphology driven by *CDH1* mutations. *CLDN18* encodes a tight junction protein, while *ARHGAP26/6* function as RHOA inhibitors, and the *CLDN18-ARHGAP26/6* fusion appears to enhance the migration and chemoresistance of gastric cancer cells, features consistent with the clinical characteristics of SRCC patients[9]. In contract, the potential functions of other SRCC-associated genes, including *ARID1A*, remain less well understood.

ARID1A, a core member of the SWI/SNF chromatin remodeling complex, is frequently mutated in multiple human cancers, including ovarian clear cell carcinoma (50%), uterine endometrioid carcinoma (29%), and gastric cancer (29%)[25,26]. *Arid1a* loss alone can drive invasive colon adenocarcinoma in mice, whereas it suppresses tumorigenesis in the small intestine of the Apc^{min} mice[27]. In liver cancer, *ARID1A* has been reported to promote tumor initiation but restrain progression and metastasis at later stages[28]. *ARID1A* knockout can also transform human gastric organoids[29]. However, whether and how *ARID1A* deficiency plays a functional role in SRCC, particularly its distinctive histopathology, remains to be investigated.

In this study, we develop a strategy to generate primary SRCC mouse models using genome-edited gastric organoids. We find that *Arid1a* loss promotes SRCC formation by directly impairing the secretory process and indirectly enhancing mucin gene expression.

Results

ARID1A loss cooperates with *TP53* and *PTEN* deficiency to promote SRCC initiation and progression

It is necessary to first analyze the transcriptomic profiles of SRCC patients in order to construct clinically relevant mouse models, given that gastric SRCC possesses distinct transcriptomic characteristics compared to other pathological types of gastric cancer. Thus, we analyzed genetic data from 171 cases of diffuse-type gastric carcinoma (DGC) and gastric signet ring cell carcinoma (SRCC) obtained from the cBioPortal database and found that *ARID1A* was altered in 39% of cases (66/171). Notably, *ARID1A* alterations frequently co-occurred with *TP53* (50%, 86/171) and *PTEN* (18%, 30/171) alterations (Supplementary Fig. 1a and Supplementary Dataset 1). To investigate the functional role of *ARID1A* in SRCC, we utilized a previously established gastric cancer mouse model that combines CRISPR/Cas9-mediated genome editing with organoid culture.

Since *ARID1A*, *TP53*, and *PTEN* alterations frequently co-occur in patient samples, we first generated gastric organoids from adult $Trp53^{-/-}$; Cas9-EGFP mice. We then introduced an sgRNA targeting *Pten*, thereby producing $Trp53^{-/-}$; sg*Pten* organoids. Subsequently, these organoids were transduced with either a non-targeting sgScramble (sgScr) control or sg*Arid1a*, yielding two engineered models: $Trp53^{-/-}$; sg*Pten*; sgScr (TP) and $Trp53^{-/-}$; sg*Pten*; sg*Arid1a* (TPA) organoids (Supplementary Dataset 2)[30,31]. Because the sgRNA-expressing plasmid co-expressed mCherry, successfully infected organoids exhibited red fluorescence, allowing their tracking and analysis. Mutations in *Pten* and *Arid1a* were confirmed by a T7 endonuclease I mismatch detection assay (Supplementary Fig. 1b and Supplementary Dataset 2), and loss of ARID1A protein expression was further validated by Western blotting (Supplementary Fig. 1c). Morphologically, TPA organoids exhibited more prominent hollow structures, with cavities filled with mucin as revealed by Alcian Blue-Periodic acid Schiff (AB-PAS) staining (Fig. 1a). Moreover, compared with TP organoids, TPA organoids were significantly larger and displayed enhanced proliferative capacity (Fig. 1b, c).

Meanwhile, we isolated and expanded monoclonal organoids derived from the TP and TPA gastric organoids (Supplementary Fig. 1d, e). These monoclonal organoids recapitulated the phenotypes observed in polyclonal cultures: TPA clones exhibited significantly increased proliferation and distinct morphological features compared with TP clones (Supplementary Fig. 1f, g). Collectively, these results indicate that monoclonal TPA organoids are phenotypically comparable to bulk TPA organoids, further indicating our strategy for investigating the function of *ARID1A*.

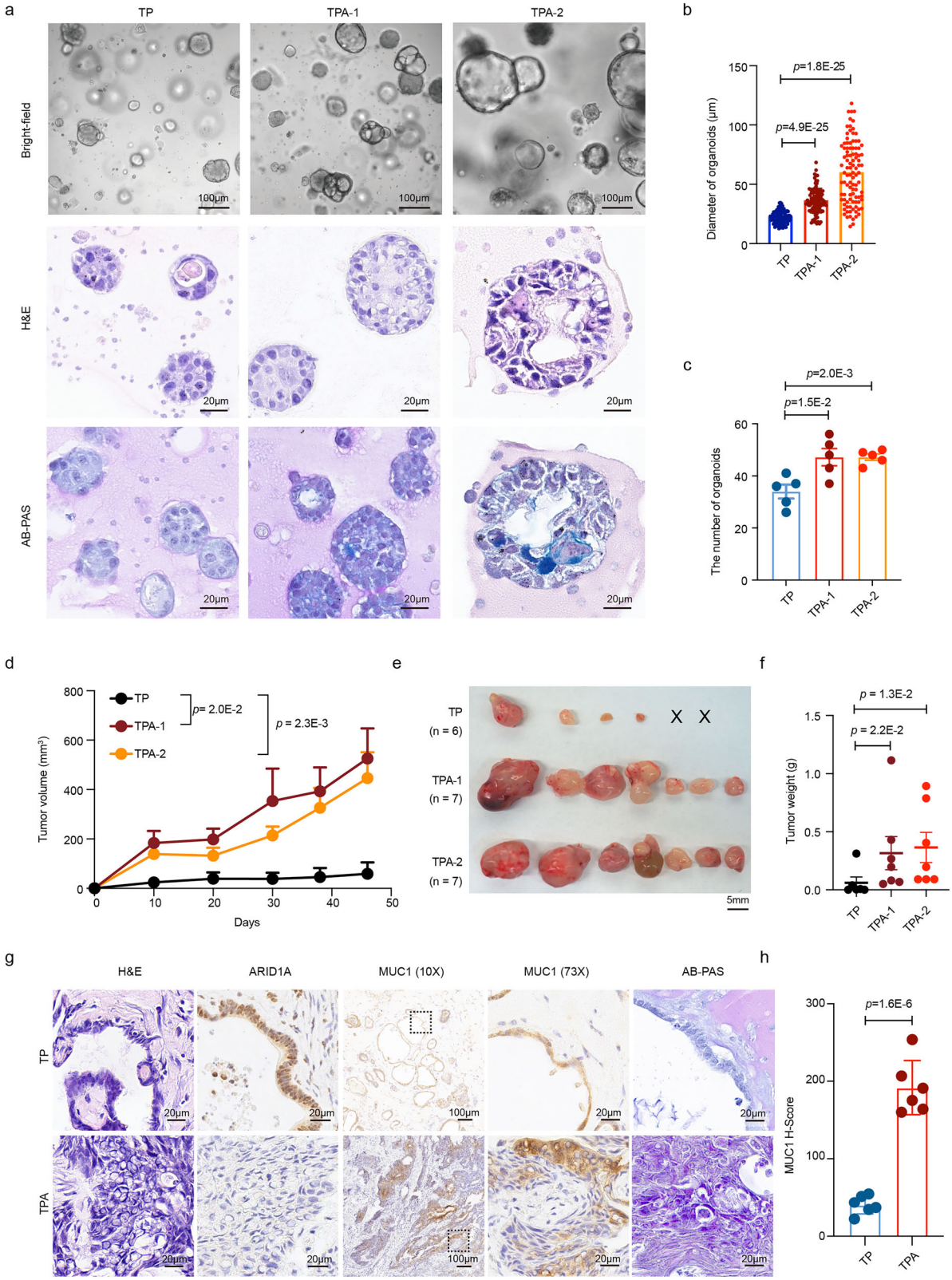
To further elucidate the role of *Arid1a*, we performed subcutaneous transplantation of TP and TPA organoids and compared their growth rates in vivo. Loss of *Arid1a* markedly accelerated tumor growth at the subcutaneous site, whereas the control group displayed only modest expansion (Fig. 1d–f). Histopathological analysis revealed that TPA-derived tumors exhibited characteristic morphological features of SRCC, including cytoplasmic mucin accumulation and nuclear compression (Fig. 1g). Immunohistochemical (IHC) staining confirmed the loss of ARID1A and the overexpression of MUC1 in TPA tumors (Fig. 1g, h). In contrast, the TP tumors mainly displayed generalized hyperplasia. Furthermore, AB-PAS staining of tumor tissues showed a marked increase in positively stained cells in the TPA group (Fig. 1g). Together, these findings identify *Arid1a* loss as a key driver of tumor initiation and progression.

Orthotopic gastric SRCC with *Arid1a* loss displayed massive mucin production

To better understand the biological function of *ARID1A* in SRCC, we orthotopically injected TP and TPA gastric organoids into the gastric submucosa of recipient mice to model clinical gastric tumorigenesis and monitored tumor formation[32–34]. Orthotopic transplantation of TP gastric organoids exhibited minimal tumorigenic capacity, with successful engraftment observed in only one recipient mouse. In contrast, TPA organoid recipients developed robust tumors characterized by histologically confirmed invasive gastric adenocarcinoma lesions. Specifically, mice transplanted with TPA organoids developed tumors significantly faster and exhibited shorter overall survival compared with control recipients (TPA-1: median 67 days after transplantation; $p = 1.0E\text{-}4$ and TPA-2: median 142 days after transplantation; $p = 4.4E\text{-}3$, Fig. 2a). Biopsy analysis confirmed that the TPA gastric organoids gave rise to a single gastric lesion showing specific mCherry expression, indicating their origin from the transplanted organoids (Fig. 2b). *Arid1a* deficiency significantly enhanced tumor growth (Fig. 2c), and tumor cells harvested from transplanted mice showed significant downregulation of ARID1A in the TPA group compared with the TP group (Fig. 2d).

To clarify the pathological classification of TPA tumors, we performed hematoxylin and eosin (H&E) staining, which serves as a key diagnostic criterion for tumor type identification. The results showed that the lesions were predominantly composed of tumor cells with prominent cytoplasmic vacuoles and eccentrically displaced crescent-shaped nuclei, consistent with the typical morphology of SRCC (Fig. 2e, f). Furthermore, AB-PAS staining revealed marked mucin enrichment within the cytoplasm of most tumor cells (Fig. 2e). Given that mucin accumulation in SRCC is readily detectable by transmission electron microscopy (TEM)[11], we next performed TEM analysis of TP and TPA tumor tissues. TEM revealed numerous cytoplasmic vacuoles with nuclei compressed to the periphery-defining ultrastructural characteristics of SRCC (Fig. 2e). IHC analysis further showed that MUC1, a mucin family protein, was markedly upregulated in TPA tumors compared with TP tumors

https://doi.org/10.1038/s41467-026-73933-0



(Supplementary Fig. 2a, b). In contrast, the epithelial differentiation marker E-cadherin (CDH1) exhibited comparable expression levels between TP and TPA tumor cohorts (Supplementary Fig. 2a, b), suggesting that the underlying mechanism of *ARID1A*-deficient SRCC may not involve the *CDH1* deficiency pathway[35,36]. Consistent with the features observed in clinical SRCC patients, TPA tumors displayed metastatic potential to distal sites, whereas no detectable metastases were observed in TP tumors (Supplementary Fig. 2c, d). The metastatic lesions exhibited the same signet ring cell carcinoma morphology as the primary tumors (Supplementary Fig. 2c, d).

Collectively, these results demonstrate that the *ARID1A*-deficiency-driven orthotopic SRCC-like model faithfully recapitulates the histological and pathological features of human SRCC.

Fig. 1 | *Arid1a* deficiency elicits the manifestation of SRCC features both in vivo and in vitro. a Representative bright-field (top), H&E (middle), and AB-PAS staining (bottom) images of TP, TPA-1, and TPA-2 mouse gastric organoids (−1 and −2 represent two independent sgRNAs targeting *Arid1a*). Scale bars, 100 μm (top) and 20 μm (middle and bottom). **b** Quantification of the diameters of TP, TPA-1, and TPA-2 gastric organoids ($n = 100$ organoids). **c** Statistical analysis of organoid formation numbers in TP, TPA-1, and TPA-2 gastric organoids ($n = 5$ biological replicates). **d** Growth curves of subcutaneously transplanted TP ($n = 6$ mice), TPA-1 ($n = 7$ mice), and TPA-2 ($n = 7$ mice). Tumor growth curves were analyzed by two-way ANOVA. **e** Representative bright-field images of subcutaneous tumors derived from TP ($n = 6$ mice), TPA-1 ($n = 7$ mice), and TPA ($n = 7$ mice). "X" denotes TP group without detectable tumor formation. Scale bar, 5 mm. **f** Tumor weight of subcutaneously transplanted TP ($n = 6$ mice), TPA-1 ($n = 7$ mice), and TPA-2 ($n = 7$ mice). **g** Representative H&E, ARID1A, MUC1 immunohistochemistry (IHC), and AB-PAS staining of subcutaneous tumors of TP (left) and TPA (right) mice. Scale bars, 100 and 20 μm. Boxed areas indicate higher magnification views. **h** The quantification of MUC1 expression in TP and TPA subcutaneous tumors tissues ($n = 6$ biological replicates). Data are shown as means ± SEM, and p-values were determined by unpaired two-tailed t-test (**b**, **c**, **f**, **h**). Source data are provided as a Source Data file.

ARID1A deficiency disrupts *SCIN*-dependent secretion in SRCC

To assess the molecular similarity between our SRCC mouse model and patient samples, we first performed RNA-seq analysis on organoids derived from TP and TPA tumor tissues. Our TPA mouse model exhibited a high degree of transcriptomic similarity to clinical SRCC patient samples (Fig. 3a and Supplementary Dataset 3). The shared upregulated genes were significantly enriched in several hallmark cancer pathways, including HALLMARK_EPITHELIAL_MESENCHYMAL_TRANSITION, GO_TISSUE_REMODELING, and KEGG_MAPK_SIGNALING_PATHWAY, among other (Fig. 3b). Moreover, gene set enrichment analysis (GSEA) revealed that genes upregulated in TPA tumors relative to TP tumors were significantly enriched in SRCC patient datasets, whereas downregulated genes were significantly enriched in intestinal-type gastric cancer (ITGC) patients (NES = 1.96, $p < 0.001$ and NES = −1.35, $p = 0.04$, respectively) (Fig. 3c).

We further performed RNA-seq on TP and TPA monoclonal organoids. Principal component analysis (PCA) revealed that the transcriptomes of TPA clones were clearly distinct from those of TP clones (Supplementary Fig. 3a), with monoclonal TPA organoids clustering together with bulk TPA organoids, and monoclonal TP organoids clustering with bulk TP organoids. Notably, the upregulated mucin genes identified in TPA monoclonal organoids were markedly increased (Supplementary Fig. 3b). GSEA further demonstrated that genes up or downregulated in bulk TPA organoids were correspondingly enriched in TPA clones relative to TP organoids (Supplementary Fig. 3c). Collectively, these phenotypic and molecular results indicate that monoclonal TPA organoids closely resemble bulk TPA organoids (Supplementary Fig. 1d–g), thereby validating our strategy for investigating the biological function of *ARID1A*.

Signet ring cells are defined by excessive intracellular mucin accumulation; however, how ARID1A contributes to this phenotype remains unknown. Based on this SRCC phenotype, we hypothesized that it results from both increased mucin production and defective secretion (Fig. 3d). Given that ARID1A functions as a chromatin remodeler, we performed ARID1A CUT&Tag (Cleavage Under Targets and Tagmentation) analysis and identified 14,864 ARID1A-regulated genomic regions (Fig. 3e and Supplementary Dataset 6). Subsequently, we performed ATAC-seq (Assay for Transposase-Accessible Chromatin using sequencing) on TP and TPA gastric organoids and identified significantly altered chromatin accessibility between the two groups (Fig. 3f and Supplementary Dataset 5). ATAC gain regions in the TPA organoids were more frequently located in promoter regions compared with ATAC loss regions (Supplementary Fig. 3d). And the tornado plots showed that the ATAC maintain regions had much less ARID1A binding than those with ATAC loss or gain, suggesting that they were not regulated by *ARID1A* (Supplementary Fig. 3e). GO enrichment analysis revealed that genes within ATAC loss regions were enriched in pathways related to epithelial differentiation and epidermal development, whereas genes within ATAC gain regions were enriched in ERK, TGF-β, and other growth-related signaling pathways (Supplementary Fig. 3f, g). Notably, analysis showed that 56.6% of genes with decreased chromatin accessibility upon *Arid1a* knockout were directly bound by ARID1A (Fig. 3f, g and Supplementary Dataset 5, 6). These genes were enriched in pathways related to gastric gland morphogenesis, including epithelial cell proliferation and gland development (Fig. 3h).

Among these genes, *Scin* (*Scinderin*)—an exocytosis-related gene that encoding an actin-severing protein essential for vesicular trafficking[37]—was directly regulated by ARID1A (Fig. 3i and Supplementary Dataset 5 and 6) and significantly downregulated following *Arid1a* loss (Fig. 3j). Consistently, analysis of the TCGA-STAD cohort revealed significantly reduced *SCIN* expression in *ARID1A*-mutant tumors compared with *ARID1A* wild-type controls (Fig. 3k). To determine whether *ARID1A* directly regulates *Scin* and its potential influence on the extracellular secretory pathway, we introduced *Scin* mutations into TP tumor organoids using CRISPR/Cas9-mediated gene editing, generating TP-sgScr and TP-sg*Scin* models (Supplementary Fig. 3h). We quantified the size and numbers of tumor organoids with sgScr or sg*Scin*. The results showed that there were more organoids with *Scin* loss than the control and they also had significantly increased size, comparing the sgScr ones (Supplementary Fig. 3i, j). Subsequently, we assessed their morphological changes. TP-sg*Scin* organoids exhibited a vacuolar phenotype accompanied by mucin overexpression (Fig. 3l, m). Moreover, TP-sg*Scin* organoids displayed a significantly higher frequency of SRCC-like morphological features compared with TP-sgScr controls (Fig. 3n).

To further investigate whether *ARID1A* directly regulates *SCIN*, we performed RNA-seq analyses to compare the transcriptomic similarity between TPA and TP-sg*Scin* tumor organoids. Loss of *Scin* in TP organoids led to gene expression changes that significantly overlapped with those in TPA organoids (Supplementary Fig. 3k). In particular, both *Scin*- and *Arid1a*-deficient organoids shared a set of downregulated genes predominantly involved in protein transport, localization, and secretion (Supplementary Fig. 3l). Collectively, these results suggest that *ARID1A* directly regulates *SCIN*. The loss of this regulation impairs normal cellular secretion, thereby contributing to the initiation of SRCC.

ARID1A deficiency directly induces *SCIN* downregulation and disrupts cellular secretion

To investigate the relationship between *ARID1A*, its direct regulation of *SCIN*, and the potential role of altered cellular secretion in SRCC pathogenesis, we performed a series of in vivo experiments. First, TP-sgScr and TP-sg*Scin* organoids were subcutaneously transplanted into mice. The results demonstrated that *Scin* disruption promoted tumorigenesis (Fig. 4a). However, the growth of the TP-sg*Scin* tumors was considerably slower than that of TPA tumors (Fig. 4b), indicating that *ARID1A*-regulated *SCIN* alone is insufficient to fully account for the SRCC phenotype. TP-sg*Scin* tumors exhibited hallmark features of SRCC (Fig. 4c, d), including cytoplasmic vacuolization and elevated MUC1 expression (Fig. 4c, e), as confirmed by H&E staining and IHC analysis. Notably, TEM showed that the TP-sg*Scin* tumor cells displayed classic signet ring cell morphology, with massive cytoplasmic mucin vacuoles displacing the nucleus to the cell periphery (Fig. 4c), consistent with the signet ring cell phenotype observed in TPA tumors (Fig. 2e).

https://doi.org/10.1038/s41467-026-73933-0

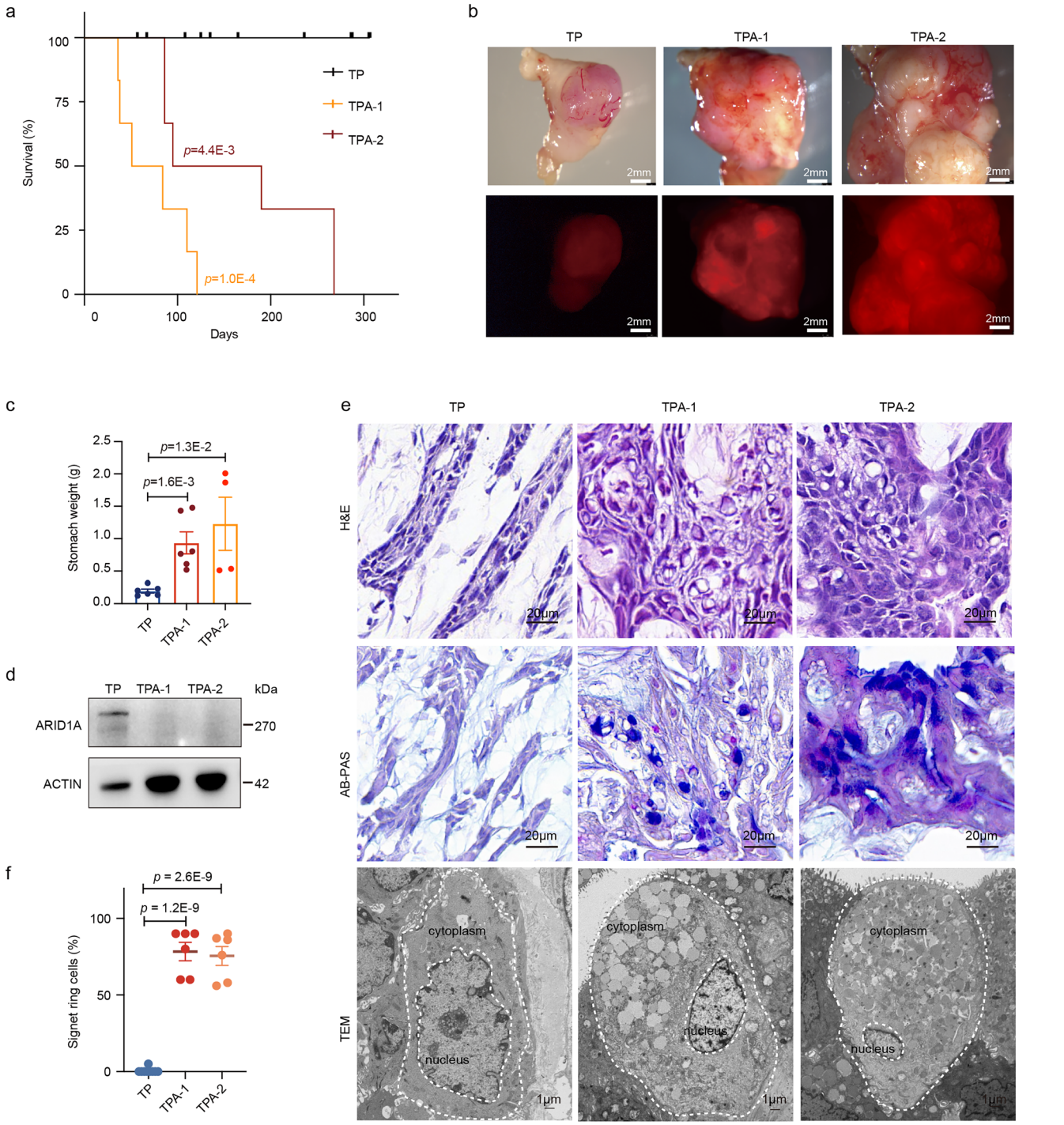
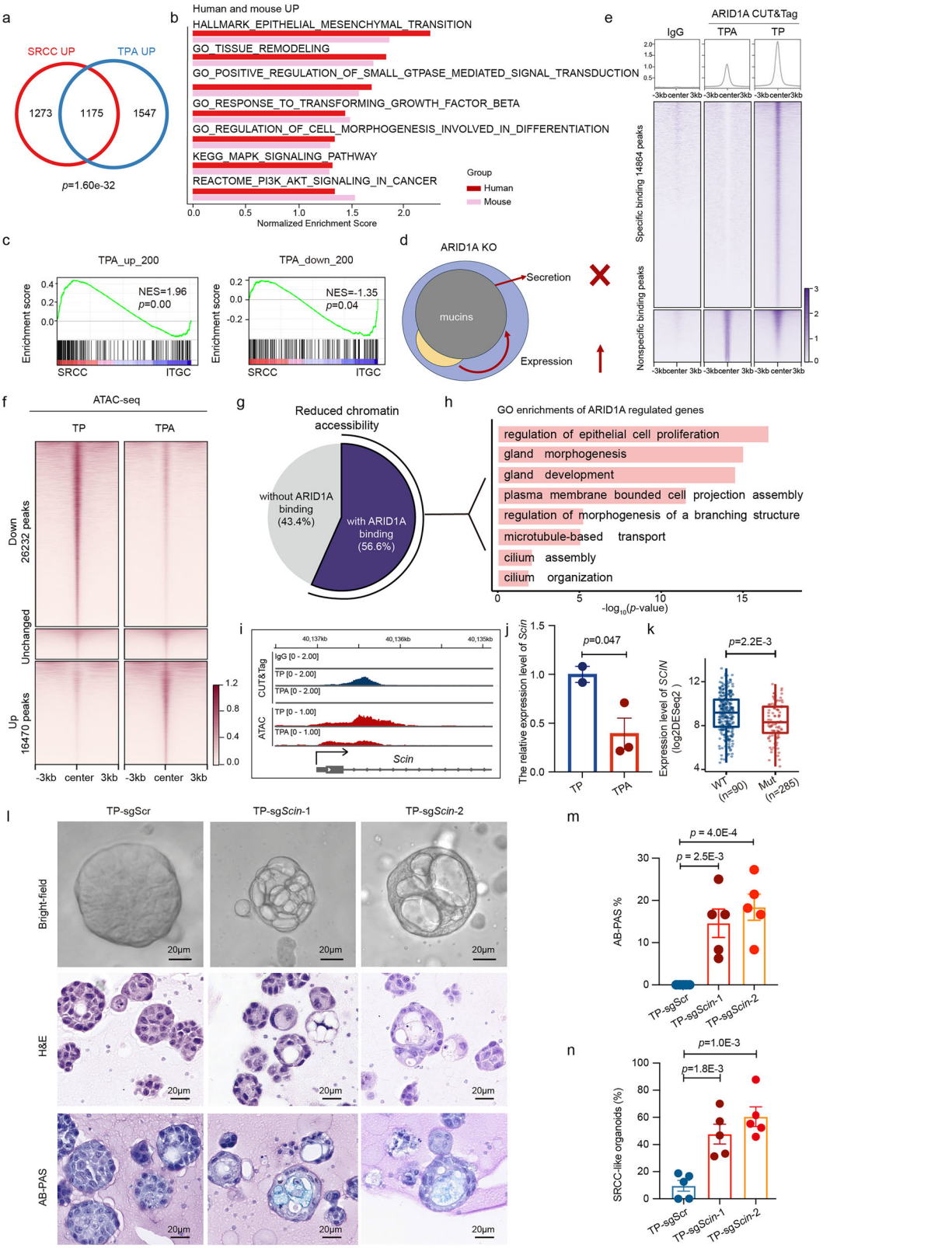


Fig. 2 | *Arid1a* deficiency markedly promotes the development of gastric SRCC. **a** Overall survival curve of mice orthotopically transplanted with TP ($n = 9$ mice), TPA-1 ($n = 6$ mice), and TPA-2 ($n = 6$ mice) organoids (−1 and −2 represent two independent sgRNAs targeting *Arid1a*). All curves were analyzed by log-rank (Mentel–Cox) test. **b** Representative bright-field (top) and red fluorescence (bottom) images of gastric cancer transduced with TP, TPA-1, and TPA-2 organoids. Scale bar, 2 mm. **c** Tumor weight of mice orthotopically transplanted with TP ($n = 6$ mice), TPA-1 ($n = 6$ mice), and TPA-2 ($n = 4$ mice) organoids. **d** Western blot analysis of ARID1A in TP, TPA-1, and TPA-2 gastric tumor organoids (−1 and −2 represent two independent sgRNAs targeting *Arid1a*). **e** Representative H&E (top), AB-PAS (middle) staining, and transmission electron microscope (TEM) (bottom) image of gastric tumor sections from TP, TPA-1, and TPA-2 mice. Scale bars, 20 and 1 μm. White dashed lines indicate cell and nuclear, respectively. **f** Box plot showing the signet ring cell percentages of TP ($n = 9$ mice), TPA-1 ($n = 6$ mice), and TPA-2 ($n = 6$ mice) tumor tissues. Data are shown as means ± SEM, and *p*-values were determined by unpaired two-tailed *t*-test (**c**, **f**). Source data are provided as a Source Data file.

Subsequently, we performed a functional rescue experiment by overexpressing SCIN in TPA tumor cells (vector control and SCIN OE). Subcutaneous xenograft assays demonstrated that *SCIN* overexpression significantly attenuated tumor growth (Fig. 4f–h). Consistent with this observation, SCIN overexpression in tumor tissues resulted in reduced signet ring cell content and diminished mucin accumulation compared with vector controls (Supplementary Fig. 4a).

Collectively, these findings suggest that *ARID1A* directly regulates *SCIN* transcription, which influence mucin secretion and thereby affect the development of SRCC.

https://doi.org/10.1038/s41467-026-73933-0



ARIDIA loss increased the expressions of mucins through a BRD9-mediated indirect mechanism

Since *Arid1a* is an ATP-dependent chromatin helicase, its loss is expected to downregulate its direct downstream targets, as we showed above in the case of *Scin* and other contexts[37]. The increased expression of mucins in TPA tumors (Fig. 5a, Supplementary Fig. 3b, and Supplementary Dataset 4) should be regulated by *Arid1a* through an indirect mechanism. Notably, emerging evidence suggests that the *ARIDIA*-containing cBAF may compete with other BAF complexes, including the BRD9- containing ncBAF[38]. We thus hypothesized that *Arid1a* loss might lead to increased activity of the BRD9-containing ncBAF, which in turn could upregulate mucin expression (Fig. 5b).

To test this hypothesis, we first measured the chromatin binding of BRD9 in TP and TPA organoids using CUT&Tag (Supplementary

Fig. 3 | Multi-omics integration reveals the loss of *Arid1a* leads to downregulation of certain genes. a Venn diagrams showing the number of overlapping upregulated pathways identified in SRCC and diffuse-type gastric cancer from the TCGA-STAD cohort (relative to intestinal-type gastric cancer) and in TPA tumor organoids (relative to TP tumor organoids). **b** Bar plots showing the top pathways commonly upregulated in SRCC and diffuse-type gastric cancer tissues from the TCGA-STAD cohort (relative to intestinal-type gastric cancer) and in TPA tumor organoids (relative to TP tumor organoids). **c** GSEA showing the TPA upregulated and downregulated gene sets compared with TP tumor organoids, significantly enriched in SRCC patients ($n = 12$) and ITGC patients ($n = 74$), respectively. *P*-values were calculated by gene-set permutation testing using the GSEAPreranked function. **d** Schematic representation of the working hypothesis: *Arid1a* deficiency results in elevated mucin expression coupled with defective secretion. **e** Tornado plot showing CUT&Tag signal levels of IgG and ARID1A in TP and TPA organoids. Scale bars represent BPM (bins per million). **f** Tornado plots showing the differential accessible genome regions in TP and TPA tumor organoids (*p*-value < 0.05, absolute $\log_2$fold-change > 1, basemean > 10, and width <10000). **g** Pie charts depicting the distribution of ARID1A-bound versus non-bound peaks within genomic regions showing reduced chromatin accessibility. **h** Gene Ontology enrichment results of ARID1A binding genes across reduced accessibility genomic regions. *P*-values were calculated using the hypergeometric test. **i** Integrative Genomics Viewer (IGV) tracks showing ARID1A binding and chromatin accessibility at the *Scin* locus in TP and TPA organoids. **j** Quantification of relative *Scin* expression in TP ($n = 2$ mice) and TPA ($n = 3$ mice) tumor organoids, measured by RT-qPCR. **k** Normalized expression levels of *SCIN* in ARID1A wild-type ($n = 285$) and mutant ($n = 90$) GC patients in the TCGA-STAD cohort. *P*-values were calculated using an unpaired, two-sided Wilcoxon rank-sum test. **l** Representative bright-field (top), H&E (middle), and AB-PAS staining (bottom) of TP tumor organoids with sgScr, sg*Scin*−1, and sg*Scin*−2 (−1 and −2 represent two independent sgRNAs targeting *Scin*). Scale bar, 20 μm. **m** Quantification of the percentage of AB-PAS positive cells in TP tumor organoids expressing sgScr, sg*Scin*−1, or sg*Scin*−2 ($n = 5$ biological replicates). **n** Quantification of the percentage of SRCC-like organoids derived from TP tumor organoids expressing sgScr, sg*Scin*−1, or sg*Scin*-2 ($n = 5$ biological replicates). Data are shown as means ± SEM, and *p*-values were calculated using an unpaired *t*-test with Welch's correction (**j**) and an unpaired two-tailed *t*-test (**m**, **n**). Source data are provided as a Source Data file.

Fig. 5a and Supplementary Dataset 7). Remarkably, 73.8% of genes located within regions that gained chromatin accessibility following *Arid1a* loss were bound by BRD9 (Fig. 5c). Consistently, BRD9 binding signals were significantly enhanced at a subset of genomic loci following *Arid1a* loss (Fig. 5d). Moreover, analysis of BRD9 binding within ATAC gain regions revealed a predominance of peaks with increased BRD9 occupancy (Supplementary Fig. 5b). BRD9 binding was predominantly localized to distal intergenic regions (40.66% in TP and 40.42% in TPA) and promoter regions (10.95% in TP and 22.97% in TPA) (Supplementary Fig. 5c, d). We next applied DiffBind to identify BRD9 gain, maintained, and loss regions in TPA organoids relative to TP organoids and subsequently characterized their genomic features. BRD9 gain regions exhibited increased genomic accessibility, whereas BRD9 loss regions showed decreased accessibility, suggesting that *BRD9* plays a critical role in gene regulation upon *ARID1A* loss (Supplementary Fig. 5e). Consistent with these findings, GO enrichment analysis revealed significant enrichment of cell cycle, TGF-beta, hypoxia, and growth-related pathways in BRD9 gain regions (Supplementary Fig. 5f). Of note, the regions with both ATAC and BRD9 binding gain contained multiple pro-tumor genes, such as *Meis3* and *Plcb4*, besides mucins (Supplementary Fig. 5g), which further suggest that *BRD9* may facilitate the pro-tumorigenic transcriptional programs associated with *ARID1A* loss.

Notably, genes that displayed increased chromatin accessibility upon *Arid1a* loss and were bound by BRD9 were significantly enriched in SRCC-related pathways (Fig. 5e). Integrative analysis identified 2479 genes with increased chromatin accessibility upon *Arid1a* loss that were both bound and transcriptionally regulated by BRD9. This set included mucin family genes (Fig. 5f), which exhibited enhanced BRD9 occupancy, elevated chromatin accessibility, and increased expression following *Arid1a* knockout (Fig. 5g, h).

To verify the mechanism by which *ARIDIA* loss increases mucin expression via an indirect BRD9 regulation, we depleted BRD9 using both genetic and chemical approaches, including sgRNA-mediated knockout and dBRD9-induced degradation strategies[39,40]. *Brd9* knockout resulted in the downregulation of *Muc1* and *Muc5ac* transcription in TPA tumor organoids (Fig. 6a and Supplementary Fig. 6a). Subsequently, we treated TP and TPA tumor organoids with dBRD9, a specific BRD9 inhibitor, in vitro. Consistent with *Brd9* knockout, *Muc1* and *Muc20* transcript levels were reduced in TPA tumor organoids, whereas TP tumor organoids exhibited no significant changes (Fig. 6b and Supplementary Fig. 6b). Moreover, dBRD9 treatment reversed the aberrant transcriptional activation of SRCC signature genes in TPA tumor organoids (Fig. 6c and Supplementary Dataset 1). Further, we performed a BRD9 CUT&Tag assay in the TPA tumors treated with or without dBRD9. The results showed that among the downregulated genes were *Muc1* and *Muc20*, which supported that BRD9 could directly regulate the expressions of mucins and that dBRD9 treatment effectively reversed the upregulation of mucins in the TPA tumors (Supplementary Fig. 6c).

To evaluate the therapeutic potential of BRD9 degradation for SRCC, we found that dBRD9 exerted a stronger effect than 5-Fu in TPA tumor organoids, which were relatively resistant to conventional chemotherapy (Fig. 6d and Supplementary Fig. 6d). Furthermore, dBRD9 treatment induced significant regression of the histological and morphological features of TPA tumor organoids, including reduced structural complexity, cribriform growth, and stratification (Fig. 6e), whereas TP organoids remained unaffected (Supplementary Fig. 6e). The proportion of SRCC-like and AB-PAS-positive organoids was significantly decreased in the dBRD9-treated groups compared with dimethyl sulfoxide (DMSO)-treated controls (Fig. 6f, g).

We further assessed the efficacy of dBRD9 treatment in vivo using *Arid1a*-deficient SRCC mouse model (Fig. 6h). TPA tumor organoids were subcutaneously transplanted into recipient mice, followed by daily treatment with either vehicle or dBRD9 (50 mg/kg). dBRD9 treatment significantly inhibited the growth of *Arid1a*-deficient tumors (Fig. 6i). Histological analysis using H&E and AB-PAS staining revealed that BRD9 inhibition reduced the proportion of signet ring cells compared with the vehicle-treated group (Fig. 6j, k). The data presented herein suggest that BRD9 inhibition represents a promising therapeutic strategy for modulating the morphological and biological characteristics of SRCC.

Collectively, these data suggest that BRD9 inhibition represents a promising therapeutic strategy for modulating the morphological and biological characteristics of SRCC. This finding is particularly significant, as current treatment guidelines for gastric adenocarcinoma lack effective options for managing SRCC. Targeting BRD9 may thus offer a novel approach to improve therapeutic outcomes for patients with this challenging gastric cancer subtype.

Discussion

Gastric SRCC is a subtype of gastric malignancies, and its study has been hindered by limited animal models. Here, we applied a recently developed strategy with genome-edited organoids to generate primary, orthotopic, and genetic drivers-defined SRCC models in mice. Similar strategies, referred to as Genetically Engineered Organoid-initiated Mouse Models (GEOMMs), have been applied to other malignancies, including lung, esophageal, bladder, and colorectal[30,31,41,42]. Recently, we also developed GEOMMs of gastric adenocarcinoma and found that different genetic alterations and microenvironments can significantly

https://doi.org/10.1038/s41467-026-73933-0

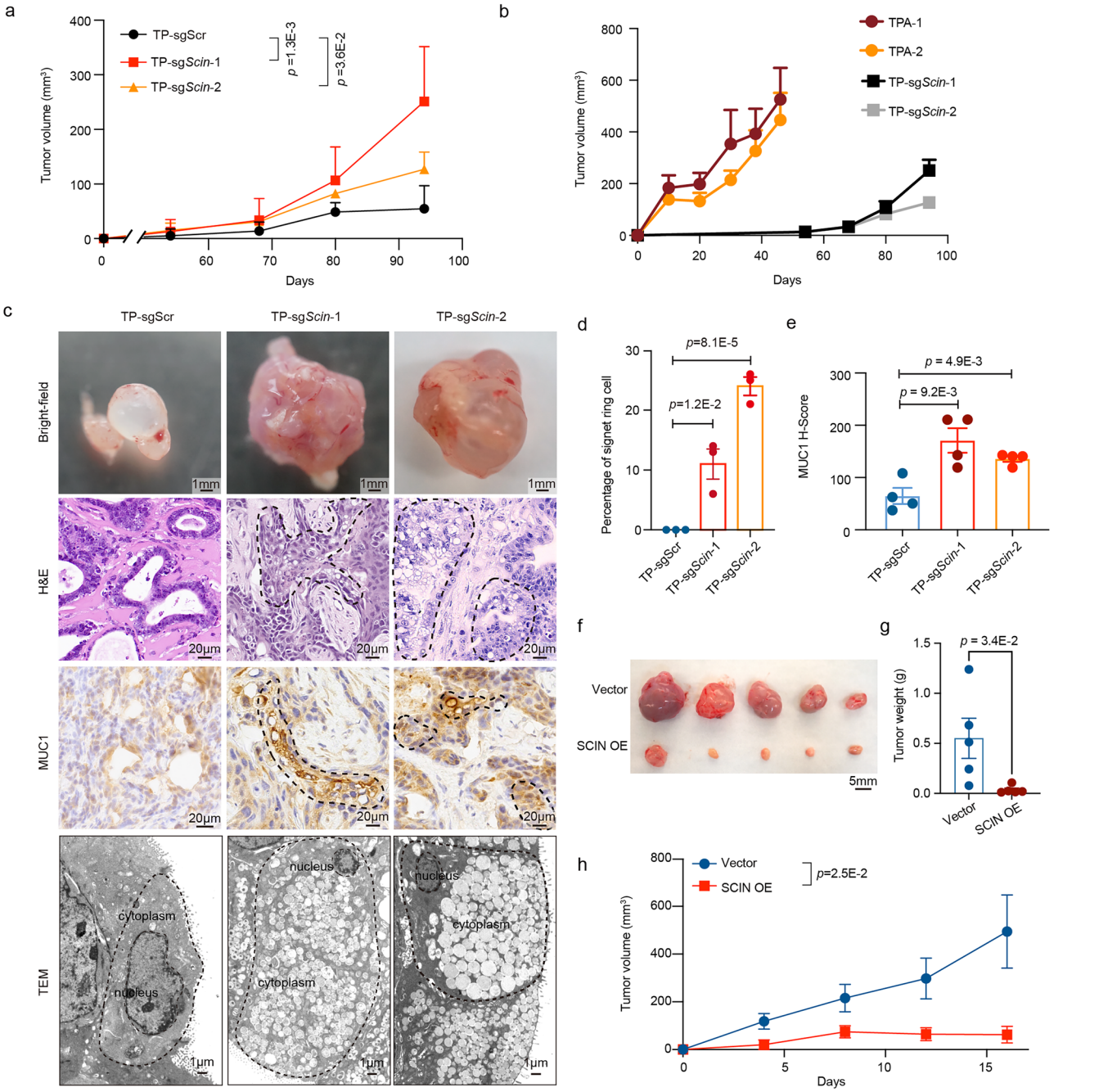
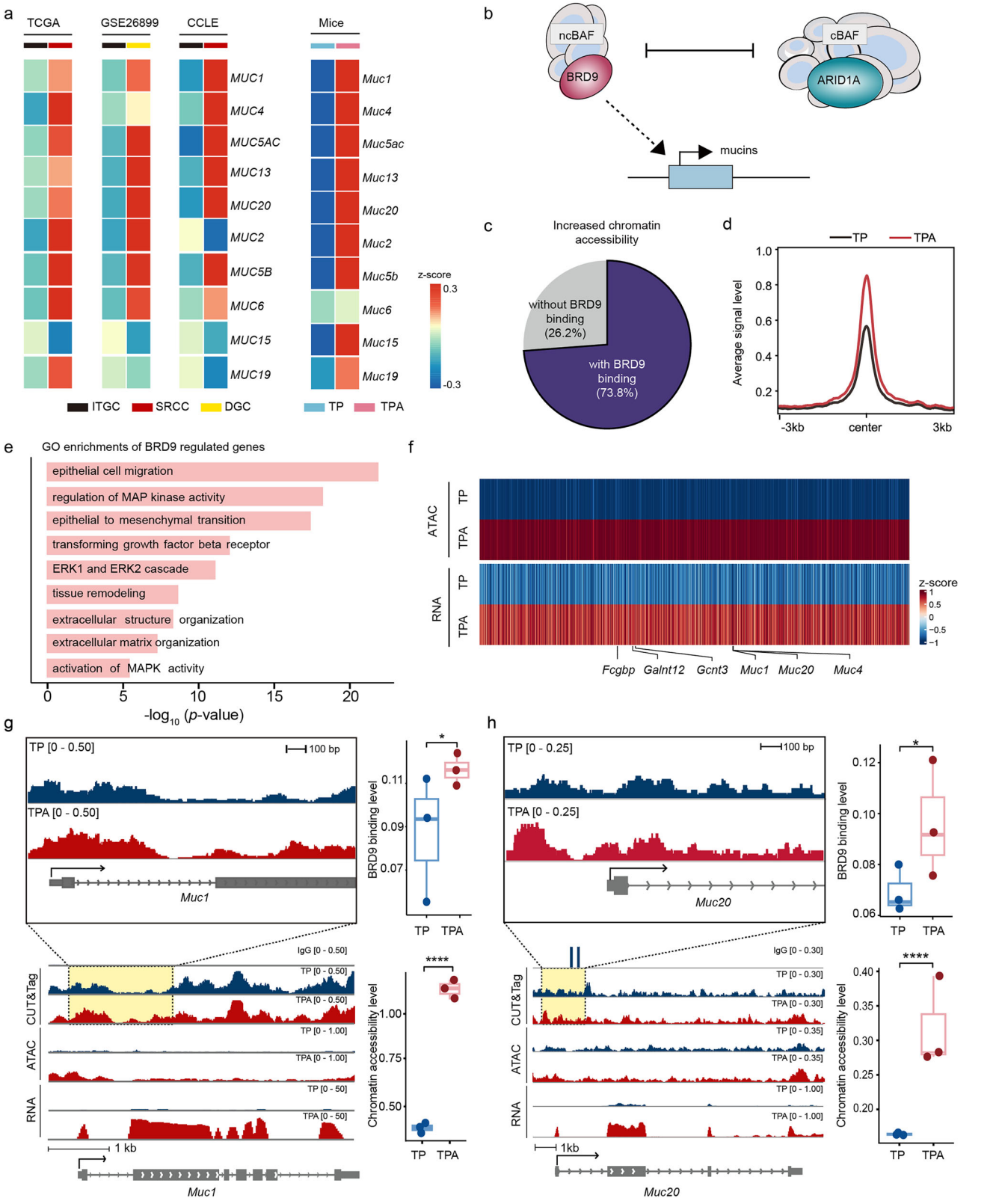


Fig. 4 | *Arid1a* suppresses SRCC by regulating the expression of secretory gene *Scin*. **a** Growth curves of subcutaneous tumors from TP tumor with sgScr ($n = 6$ mice), sg*Scin*−1 ($n = 6$ mice), and sg*Scin*−2 ($n = 3$ mice). **b** Growth curves of subcutaneous tumors from TPA-1 ($n = 7$ mice), TPA-2 ($n = 7$ mice), TP tumors with sg*Scin*−1 ($n = 6$ mice), and sg*Scin*−2 ($n = 3$ mice) (−1 and −2 represented two independent sgRNAs targeting *Arid1a* and *Scin*, respectively). **c** Representative images of bright-field, H&E, MUC1 IHC staining, and TEM images of TP tumor with sgScr, sg*Scin*−1, and sg*Scin*−2. Scale bars, 1 mm, 20 μm, and 1 μm. Black dashed lines indicate signet ring cell in the H&E and MUC1 IHC images. Black dashed lines indicate cell and nuclear in the TEM images, respectively. **d** Quantification of the percentage of signet ring cells in TP tumor tissues with sgScr, sg*Scin*−1, and sg*Scin*−2 ($n = 3$ mice). **e** The quantification of MUC1 expression from TP tumor with sgScr, sg*Scin*−1, and sg*Scin*−2 ($n = 4$ biological replicates). **f** Bright-field image of subcutaneous tumors from TPA tumor with vector ($n = 5$ mice) and *SCIN* ($n = 5$ mice). Scale bar, 5 mm. **g** Tumor weight of subcutaneous tumors from TPA tumor with vector ($n = 5$ mice) and *SCIN* ($n = 5$ mice). **h** Growth curves of subcutaneous tumors from TPA tumor with vector ($n = 5$ mice) and *SCIN* ($n = 5$ mice). Data are shown as means ± SEM, and *p*-values were determined by unpaired two-tailed *t*-test (**a**, **d**, **e**, **g**, **h**). Source data are provided as a Source Data file.

influence their progression and metastasis[32]. Using a similar approach, we also established an *Ezh2*-driven mouse model of gastric squamous cell carcinoma[34]. Compared with conventional genetically engineered mouse models (GEMMs), GEOMMs provide a more efficient platform for functional characterization of novel genetic alterations. This advantage makes them valuable for dissecting the functions of the numerous human cancer-associated genes revealed by cancer genomics studies.

Using this strategy, we found that gastric organoids with *Arid1a* loss, together with *Trp53* and *Pten* deficiencies, exhibited tumor characteristics of SRCC when implanted both subcutaneously and orthotopically in the stomach. These findings not

https://doi.org/10.1038/s41467-026-73933-0



only validate *ARID1A*, one of the most frequently mutated genes in SRCC, as a bona fide tumor suppressor of gastric SRCC in mice but also provide a strategy for investigating the functions of other SRCC-associated genes. We found that *CDH1* also plays an important role in SRCC. However, we didn't observe a significant change of CDH1 levels in the TPA tumors, which was consistent with the IF staining results reported by ref. 29. Only about 10% gastric SRCC patients have CDH1 mutations[9,16]. And single cell RNA-seq analyses found that "it was revealed that the CDH1 expression level was essentially the same between M/PDA and SRCC cells"[14]. Despite the unchanged CDH1 levels, the TPA tumors displayed typical SRCC histopathological features, including intracytoplasmic mucins and nucleus pushed to the edge and these SRCC-like cells consisted of about 80% of all tumor cells. We also observed increased

Fig. 5 | Multi-omics integration reveals coordinated BRD9-driven gene activation following *ARID1A* loss. a Heatmap showing the expression levels of mucin genes in SRCC, diffuse-type gastric cancer (DGC), and intestinal-type gastric cancer (ITGC) patients from the TCGA-STAD cohort; the Korea University cohort (GSE26899); the CCLE database; and TP and TPA tumor organoids. **b** Schematic representation of the working hypothesis, in which *Arid1a* deficiency results in elevated mucin expression. **c** Pie charts depicting the distribution of BRD9-bound versus non-bound peaks within genomic regions showing increased chromatin accessibility. **d** Intensity curves showing the average BRD9 signal across regions with significantly increased BRD9 binding in TPA compared with TP gastric organoids. **e** Gene Ontology enrichment analysis of genes associated with BRD9 binding peaks within regions of increased chromatin accessibility. **f** Heatmap showing chromatin accessibility changes and corresponding transcriptional alterations of genes with increased accessibility and upregulated expression upon *Arid1a* knockout. Mucin production-related genes are annotated. **g** Integrative Genomics Viewer and box plots showing the BRD9 binding, accessibility, and expression levels of *Muc1* gene between TP and TPA organoids ($n = 3$ biological repeats). **h** Integrative Genomics Viewer and box plots showing the BRD9 binding, accessibility, and expression levels of *Muc20* gene between TP and TPA organoids ($n = 3$ biological repeats). In this figure (**g** and **h**), center lines indicate the median, box bounds indicate the 25th and 75th percentiles, and whiskers extend to the smallest and largest observations within 1.5 × IQR from the hinges. *P*-values were determined by the hypergeometric test in this figure (**e**) and by the two-sided likelihood ratio test in this figure (**g** and **h**).

metastases in the TPA mice, consistent with the features observed in clinical SRCC patients[14].

ARID1A is frequently disrupted in many other types of human cancers as well[43–45]. However, its roles and underlying mechanisms in tumorigenesis and progression are complex and context-dependent. For example, *ARID1A* exhibits opposing functions in the initiation and progression of liver cancer through regulating oxidative stress and chromatin accessibility, respectively[28]. In liver cholangiocarcinoma, *Arid1a* loss cooperates with *Kras* mutation to promote tumorigenesis via repression of the TGF-β pathway[46], whereas activation of the YAP pathway is essential for *Arid1a* deficiency-induced pancreatic ductal adenocarcinoma[47]. In the urothelium, *ARID1A* loss induces a transcriptional-translational conflict, resulting in uncontrolled proliferation, clonogenic growth, and bladder cancer progression[48].

Given the well-characterized roles of the *ARID1A*-containing SWI/SNF complex in chromatin remodeling and transcriptional regulation, *ARID1A* loss has been expected to cause a global reduction in chromatin accessibility[28,29,49]. However, accumulating evidence indicates that, at least in some tumors, *ARID1A* deficiency instead increases chromatin accessibility, possibly through the dysregulation of other chromatin remodeling factors[50–52]. Consistently, our study demonstrates that *Arid1a* loss led to hyperproliferation in our model, which is consistent with previous studies in many other types of cancers, while the detailed mechanisms were context-dependent[28,29,53]. GSEA and RNA-seq analyses revealed that TPA tumors displayed significantly enriched gene signatures related to MAPK and PI3K-AKT signaling, consistent with transcriptional activation of these pathways. Comparable signatures were also observed in SRCC patients and were associated with cell proliferation. In particular, we found that secretory genes such as *Scin* were directly downregulated, while mucin genes were indirectly increased in *Arid1a*-loss-induced SRCC. This mechanism differs from that reported by Lo et al., who showed that combined *ARID1A* and *TP53* loss drove diffuse gastric cancer in human gastric organoids but did not observe an SRCC-like phenotype[29]. Interestingly, their Alcian blue staining revealed mucin proteins predominantly localized to the organoid lumen, whereas in our models, AB-PAS staining demonstrated marked intracellular mucin retention together with transcriptional and epigenomic evidence linking ARID1A loss to mucin regulation. Although the precise basis for these differences remains unclear, potential explanations include distinct genetic contexts (*TP53* loss alone versus combined *Trp53* and *Pten* loss), the accumulation of unidentified mutations during prolonged organoid culture.

Given the prevalence and tumorigenic functions of *ARID1A* mutations, there has been attractive to explore potential therapeutic strategies for *ARID1A*-altered tumors. Previous studies have shown that *ARID1A*-inactivated ovarian carcinomas exhibit defects in the mevalonate pathway and are therefore sensitive to statin treatment, alone or in combination with immune checkpoint blockade[54]. Multi-omics analyses have suggested that *ARID1A*-mutated gastric cancers may be responsive to bromodomain and NF-κB inhibition[55]. We found that *Arid1a* loss leads to *Brd9*-mediated upregulation of mucin genes. Thus, we propose that targeting *Brd9* or the non-classic BAF complex may represent an effective therapeutic strategy for SRCC, which is characterized by excessive mucin accumulation. Our finding are consistent with observations in other cancer types, including sarcoma[39], rhabdoid tumor[56], and liver cancer[57]. It will be of great interest to test inhibitors of the non-classic BAF complex in patients harboring *ARID1A* mutations. Nevertheless, we also note that *ARID1A* may play complex roles in both malignant cells and nonmalignant cells, such as its function in tumor-infiltrating T cells[58]. Therefore, therapeutic strategies targeting *ARID1A*-deficient tumors should be carefully evaluated for potential systemic effects.

Methods

Ethics statement

For studies involving mice described below, all animal procedures were approved by the Institutional Animal Care and Use Committee (IACUC) of West China Hospital. The maximal tumor volume permitted under the approved protocol was 1500 mm^3. Tumor size was monitored regularly throughout the study, and no tumors from any mice exceeded this predefined limit.

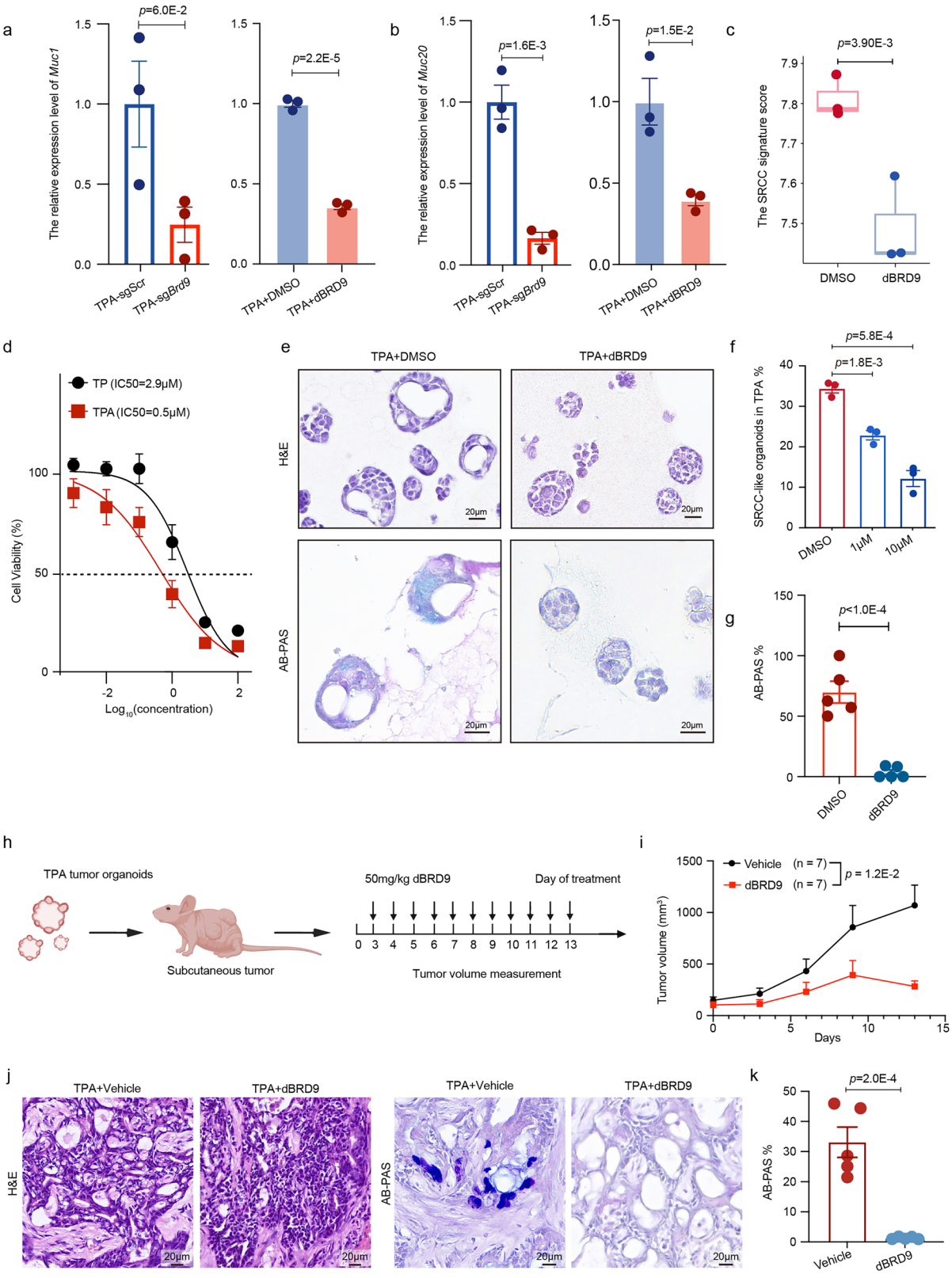
Mice

All these mice were bred and kept in the SPF animal facility of Sichuan University, and no mouse was excluded in the experiments. *Trp53*$^{-/-}$ mice from The Jackson Laboratory (Stock No: 002101, RRID: IMSR_JAX:002101) and *Trp53*$^{-/-}$; Cas9-expressing mice obtained by breeding *Trp53*$^{-/-}$ mice with *Cas9* knock-in mice from The Jackson Laboratory (Stock No: 026179, RRID: IMSR_JAX:026179) were served as donor mice (both in C57BL/6 background). BALB/cA-nu mice were purchased from Beijing HuaFukang Biological Technology Co., Ltd. (6–8-week-old).

Mouse organoid culture

Mouse organoid cultures were established and maintained as described previously[32]. Specifically, normal mice stomach was mechanically minced into pieces of 5-mm^3 cubes and incubated in DPBS with 2.5 mM EDTA on ice. After incubation, the released gastric gland fractions were resuspended with Matrigel (Corning, Cat# 356237) and seeded in 48-wells plate. Tumor tissues were harvested and washed with ice-cold DPBS, and then minced into pieces. Incubating the minced tumor tissue in digestion medium containing 0.5 mg/ml collagenase IV (GIBCO, Cat# 17104-019) and 1.0 mg/ml collagenase I (GIBCO, Cat# 17100-017) in DMEM/F12 medium at 37 °C until it dissociates into single cells or cell clusters. Tumor cells were collected by centrifugation and resuspended with Matrigel. Organoid culture medium was DMEM/F12 (GIBCO, Cat# C11330500BT) supplemented with 2 mM GlutaMAX (GIBCO, Cat# 35050-061), 1% Penicillin and Streptomycin (GIBCO, Cat# 15140-122), 1× B27 (GIBCO, Cat# A3582801), 1× N_2 (GIBCO, Cat# 17502048), 10 mM Y-27632,

https://doi.org/10.1038/s41467-026-73933-0



200 ng/ml FGF10 (Peprotech, Cat# 100-26-1000), 500 nM A-8301 (Peprotech, Cat# 9094360), 50 ng/ml mouse recombinant EGF (Peprotech, Cat# AF-100-15-1000), 100 ng/ml mouse recombinant noggin (Peprotech, Cat# 120-10C-250), 10 mM Nicotinamide (Sigma, Cat# N0636), 1 mM N-acetylcysteine (Sigma, Cat# A9165), 10% Wnt3a condition medium, 10% R-spondin1 condition medium). Organoid medium was refreshed every 2–3 days.

Organoid genome editing

sgRNAs designed on the website of DNA2.0 Gene Design & Synthesis (https://www.atum.bio/pipeline/dna) were cloned into the lentiviral constructs U6-sgRNA-EFS-mCherry-P2A-puro. Human *SCIN* cDNA sequences were obtained from the https://asia.ensembl.org/index.html, digested by BglII (Cat#R0144S) and EcoRI (Cat#R0101S) endonuclease from New England BioLabs, and followed by cloning into the

Fig. 6 | Inhibition of *BRD9* can reverse the SRCC phenotype caused by *ARID1A* loss. a Quantification of relative *Muc1* mRNA expression in TPA tumor organoids transduced with sgScr or sg*Brd9* and treated with DMSO or 10 μM dBRD9, as determined by RT-qPCR ($n = 3$ biological replicates). **b** Quantification of relative *Muc20* mRNA expression in TPA tumor organoids transduced with sgScr or sg*Brd9* and treated with DMSO or 10 μM dBRD9, as determined by RT-qPCR ($n = 3$ biological replicates). **c** Box plots showing the SRCC signature gene scores in DMSO and dBRD9 treated TPA tumor organoids. Likelihood-ratio test was used to determine the significance level. The center line indicates the median, the box bounds indicate the 25th and 75th percentiles, and the whiskers extend to the smallest and largest observations within 1.5 × IQR from the hinges. *P*-value was determined by the two-sided Likelihood ratio test. **d** Dose-response curves of TP and TPA tumor organoids treated with dBRD9 ($n = 3$ biological repeats). **e** Representative H&E (top) and AB-PAS (bottom) images of TPA tumor organoids treated with DMSO or 10 μM dBRD9. Scale bar, 20 μm. **f** Quantification of the percentage of SRCC-like organoids in TPA tumor organoids treated with DMSO, 1 and 10 μM dBRD9 ($n = 3$ biological replicates). **g** Quantification of the percentages of AB-PAS-positive cells in TPA tumor organoids treated with DMSO or 10 μM dBRD9 ($n = 5$ biological replicates). **h** Schematic diagram of the strategy for dBRD9 treatment in TPA tumor-bearing mice. Created in BioRender. Pang, X. (2026) https://BioRender.com/zy182ha. **i** Growth curves of the TPA subcutaneous tumors treated with vehicle or dBRD9 ($n = 7$ mice). Tumor growth curves were analyzed by two-way ANOVA. **j** Representative H&E (left) and AB-PAS (right) images of the TPA tumors treated with dBRD9 and vehicle. Scale bar, 20 μm. **k** Quantification of the percentages of AB-PAS positive regions in the TPA tumors treated with vehicle or dBRD9 ($n = 5$ biological replicates). Data are presented as mean ± SEM, and *p*-values were determined using unpaired two-tailed *t*-tests (**a**, **b**, **f**, **g**, **k**) and a two-tailed Mann−Whitney test (**h**). Source data are provided as a Source Data file.

retroviral plasmid MSCV-cDNA-IRES-GFP. The sequences of gRNAs and primers targeting *Pten*, *Arid1a*, *Scin*, and *Brd9* are listed in Supplementary Dataset 2. Lentivirus packaging, infection, and verification were done as previously reported[31].

Generation of clonal organoid lines

After washing with PBS, organoids were dissociated using TrypLE™ dissociation reagent at 37 °C for 10 min. Cell aggregates were removed by passing the suspension through a 35 μm cell strainer, and the filtrate was centrifuged at 400 × *g* for 5 min at 4 °C to collect the cell pellet. The pellet was resuspended in culture medium supplemented with 10 μM Y-27632. Cells were then distributed into individual wells of a 96-well plate by serial dilution. The plate had been pre-coated with 10 μL of Matrigel and overlaid with 100 μL of organoid culture medium. Wells containing a single cell were confirmed by microscopic examination. After 8–10 days, wells containing a single organoid were dissociated with TrypLE™ and re-plated for clonal expansion.

Organoid subcutaneous transplantation

Trp53$^{-/-}$;sg*Pten*;sgScramble (TP) and *Trp53*$^{-/-}$;sg*Pten*;sg*Arid1a* (TPA) gastric organoids, TP-sgScramble and TP-sg*Scin* tumor organoids, TPA tumor organoids were dissociated into single cells using TrypLE™ Express, resuspended in Matrigel (Corning #356231), and mixed with PBS at a 1:1 ratio. Cell viability was confirmed >90% by trypan blue exclusion. The cell suspension (2×10^5 cells in 50 μL total volume) was aspirated into pre-chilled 29 G insulin syringes and injected subcutaneously into the right flank of 6–8-week-old BALB/cA-nu mice ($n = 6–7$ per group). Tumor growth was monitored. Tumor sizes were periodically measured using vernier calipers, and tumor volume was calculated using the formula: 0.52 × width^2 × length (mm^3). Refer to the previous article for detailed methods[32].

Organoid orthotopic transplantation

For the orthotopic model, organoids were collected and aspirated into prechilled 29 G insulin syringes. 6 to 8-week-old nude mice were continuously anesthetized via a nose cone connected to an isoflurane vaporizer. An abdominal incision was made using sterile surgical scissors, and the stomach was gently exteriorized with forceps. Organoids ($5–8 \times 10^5$ cells in 50 μL Matrigel/PBS suspension) were injected into the submucosal layer of the lower gastric corpus using a 29 G insulin syringe. The stomach was repositioned into the abdominal cavity, and the abdominal wall was closed with 5–0 sutures. Postoperative mice were monitored until fully ambulatory. Mice was monitored weekly.

H&E and immunohistochemistry staining

Tumor tissues and organoids were fixed with 4% paraformaldehyde overnight, then subjected to gradient dehydration, embedded in paraffin, and preserved at room temperature. The standard protocol was used for H&E and immunohistochemistry staining. Imaging was performed using a Pannoramic MIDI. The H-score, a semiquantitative assessment of immunohistochemical staining intensity and distribution, was calculated for each tumor sample to evaluate protein expression. The staining intensity was visually graded on a scale of 0 to 3: 0 (Negative or no staining), 1$^+$ (Weak staining), 2$^+$ (Moderate staining), and 3$^+$ (Strong staining). For each intensity grade (0, 1$^+$, 2$^+$, 3$^+$), the percentage of tumor cells exhibiting that specific intensity was estimated. The H-score was then calculated using the following formula:

$$H-\text{score} = (1 \times \%\ \text{of}\ 1^+\ \text{cells}) + (2 \times \%\ \text{of}\ 2^+\ \text{cells}) + (3 \times \%\ \text{of}\ 3^+\ \text{cells})$$

The resulting score ranges from 0 to 300, where 0 represents no staining and 300 represents strong staining in 100% of the tumor cells.

Western blotting

TP and TPA gastric organoid lysates were extracted in RIPA buffer (Beyotime, Cat# P0013) supplemented with protease inhibitors (Beyotime, Cat# P1045), followed by SDS–PAGE electrophoresis and transfer onto PVDF membranes (Millipore). Primary antibodies were applied in 5% non-fat milk and incubated overnight at 4 °C. HRP-conjugated secondary antibodies were applied at a 1:10,000 dilution. Images were obtained using NcmECL Ultra Reagent (NCM Biotech).

RNA extraction and RT-qPCR

Total RNA was extracted from TP, TPA-1, TPA-2, TP-sgScr, TP-sg*Scin*−1, TP-sg*Scin*−2, TPA-sgScr, TPA-sg*Brd9*-1, and TPA-sg*Brd9*−2 tumor organoids for RT-qPCR. Total RNA was extracted using TRIzol reagent (Thermo Fisher Scientific, Cat# 15596026), and complementary DNA (cDNA) was synthesized using the HiScript-III RT SuperMix kit (Vazyme, Cat# R323-01) according to the manufacturer's instructions. Real-time quantitative PCR (RT-qPCR) was performed using Fast SYBR Green Master Mix (Vazyme, Cat# Q711-02/03) on the StepOne Real-Time PCR System (Thermo Fisher Scientific, Applied Biosystems QuantStudio 3). *Muc1*, *Muc5ac*, mouse *Scin*, and human *SCIN* gene primers for RT-qPCR are listed in Supplementary Dataset 2.

Organoid proliferation assay

Organoids were digested into single cells using TrypLE™ (GIBCO, Cat# 12605-028). A total of 5000 cells were seeded into each well of a 96-well plate. After 5 days of culture, organoids were photographed using an Olympus IX73P2F. The size of organoids was measured using ImageJ (Version 1.51).

Antibodies

The Recombinant Anti-MUC1 antibody (Cat# ab45167, RRID: AB_776552) was obtained from Abcam; ARID1A/BAF250A (D2A8U) Rabbit mAb (Cat# 12354, RRID: AB_2637010) and E-Cadherin (4A2) Mouse mAb (Cat# 14472, RRID: AB_2728770) were obtained from Cell

Signaling Technology. The BRD9 polyclonal antibody (Cat# A303-781A, RRID: AB_11218396) was obtained from Thermo Fisher Scientific.

In vitro treatment

Tumor organoids from TP and TPA mice were dissociated using TrypLE™ and seeded into 96-well plates at a density of 5000 cells per well. After 24 h of culture, the organoids were treated with varying concentrations of dBRD9 (GlpBio, Cat# 2341840-98-8) (0, 0.001, 0.01, 0.1, 1, 10, and 100 μM). After 72 h of treatment, the organoids were photographed and quantified using CCK8. The ratio of signet ring cell organoids to total organoids was calculated from at least three independent areas. Cell viability was determined by normalizing to the DMSO group.

In vivo treatment

TPA tumor organoids was cultured and performed subcutaneous transplantation with 50,000 cells per site. Tumor volume was then monitored using vernier calipers. When the subcutaneous tumors reached approximately 100 mm^3, the mice were randomly divided into two groups for intraperitoneal drug administration: one group received vehicle control (10% DMSO + 40% PEG300 + 5% Tween-80 + 45% saline) and the other received the dBRD9 compound (*MedChemExpress*, Cat# 2170679-45-3) treatment group. Daily dosing was administered at 50 mg/kg, with tumor volume measurements recorded every three days using vernier calipers throughout the treatment period. Mice were sacrificed and analyzed at the indicated time points.

RNA-seq analysis

Total RNA was extracted from gastric TP and TPA tumor organoids, TP tumor organoids (sgScr and sgScin), and TPA tumor organoids treated with vehicle or dBRD9 for transcriptome profiling. RNA-seq libraries were sequenced on an Illumina NovaSeq 6000 platform (150-bp paired-end reads). After removing the adapters, ploy-N, and low-quality reads, clean data were aligned against the reference mouse genome (mm10) using STAR_2.6.0. Following this, raw counts were normalized and significance scores. as well as log2-fold change values, were calculated using the DESeq2 (v.1.22.2). The differentially expressed genes were used to perform Gene Ontology enrichment analyses with the R package clusterProfiler (v.3.10.1) (RRID:SCR_016884). Furthermore, Gene Set Enrichment Analysis (GSEA) was employed to identify significantly enriched pathways. Preranked function was performed to clarify the overall transcriptome similarity between mouse models and tumor tissues of SRCC patients. Data visualization was conducted using the R packages ggpubr, ggplot2, pheatmap, and Vennerable.

Constructing ATAC-seq libraries

Gastric TP and TPA organoids (5×10^4 cells/each group) were harvested to construct ATAC-Seq libraries using a Chromatin Profile Kit (Novoprotein, Cat. N248-01A). 1 mL ice-cold PBS suspended organoids, then centrifuged at 500 × *g* at 5 min. The supernatant was removed and 50 μL lysis buffer gently resuspended organoids. Tubes were placed on ice for 5 min and added into 950 μL wash buffer, then gently blown 5 times, which was centrifuged at 500 × *g* for 5 min at 4 °C. The sediment was added into a 40 μL fragmented mixture and transferred to PCR tubes for 30 min at 37 °C. Then 10 μL stop buffer was used to end the reaction for 5 min at 55 °C. The DNA extracted beads were used for purifying fragments. Transposed DNA fragments were amplified using the PCR system from this kit. PCR conditions: 72 °C for 3 min, 98 °C for 30 s, followed by 9–18 cycles of 98 °C for 15 s, 60 °C for 15 s and 72 °C for 10 s, 72 °C for 2 min. Amplified libraries were purified with the DNA Clean Beads.

ATAC-seq analysis

Assay for Transposase-Accessible Chromatin using sequencing (ATAC-seq) was performed on nuclei isolated from TP and TPA gastric organoids to profile genome-wide chromatin accessibility. The Illumina NovaSeq 6000 platform was utilized to sequence the library. To remove adapters from the 150 bp paired-end raw data, NGmerge was employed with the option "NGmerge -a -v -n 20". Bowtie2 software was used to construct an index for the mouse genome (mm10), followed by alignments using the option "–very-sensitive -X2000 -x mm10". Duplicates were removed using Picard's MarkDuplicates tool. Mitochondrial genome contamination was eliminated using SAMtools and awk commands, resulting in bam files. Normalized bw files were generated using deepTools with the option "bamCoverage -bs = 1 –normalizeUsing BPM" for subsequent visualization in the Integrated Genome Viewer (IGV). Macs3 hmmratac standard workflow was utilized for peak calling in ATAC-seq. The genomic distribution of accessibility sites was determined using ChIPseeker with the option "annotatePeak", and the TSS region "tssRegion" was set as (−3000, 3000). The "gappedPeak" files were transformed into GrangesList forms, and the peaks were converted into consensus counts. Data normalization and differential comparison were performed using DESeq2. Regions of differential accessibility were identified for downstream analyses using a *p*-value cutoff of 0.05 (Wald test).

Constructing CUT&Tag-seq libraries

Gastric TP and TPA organoids (1×10^5 cells/per group) were harvested to construct CUT&Tag libraries. TP and TPA organoids were used for BRD9 and ARID1A CUT&Tag. Organoids were harvested in 1.5 mL tubes for the CUT&Tag assay using the NOvoNGS CUT&Tag 3.0 High-Sensitivity Kit (Novoprotein, Cat. N259-YH01-01A). A total of 10 μL of ConA beads were added to each tube and incubated with cells for 10 min at 25 °C. The supernatant was removed and the primary antibody buffer with the appropriate primary antibody was added and incubated for 2 h at 25 °C or overnight at 4 °C. The supernatant was removed, and the secondary antibody buffer was added and incubated for 1 h at 25 °C. Beads were washed twice. The chromatin was combined with ChiTag™ 2.0 Transposome, then fragmented using Tagmentation Buffer for 1 h at 37 °C. ChIP DNA was purified using DNA Clean Beads and amplified using the PCR system from this kit. PCR conditions: 72 °C for 3 min, 98 °C for 30 s, followed by 10–25 cycles of 98 °C for 15 s, 60 °C for 15 s, and 72 °C for 10 s, then 72 °C for 2 min. Amplified libraries were purified using DNA Clean Beads. The purified ChIP DNA was used for library preparation.

CUT&Tag analysis

CUT&Tag (Cleavage Under Targets and Tagmentation) assays were conducted on chromatin isolated from TP and TPA gastric organoids using antibodies against ARID1A, BRD9, or control IgG. The Illumina NovaSeq 6000 platform was employed to perform genomic sequencing. Following quality control by the fastp standard workflow, the Bowtie2 software was utilized to construct an index for the mouse genome (mm10) and align paired-end clean data of 150 bp length using the options "–local –very-sensitive-local –no-unal –no-mixed –no-discordant –phred33 -I 10 -X 700". The SAMtools program was utilized to convert sam files to sorted bam files. Picard's MarkDuplicates tool was used to remove duplicates with the option "REMOVE_DUPLICATES = true". Normalized bw files were generated using deepTools with the option "bamCoverage -bs = 1 –normalizeUsing BPM" for further visualization in the Integrated Genome Viewer (IGV). Peak calling was performed using the MACS2 and MACS3 software with the option "narrow -q 1e-5 -f BAMPE -g mm –keep-dup all". ChIPseeker was employed to identify the genomic distribution of the peaks, with the TSS region "tssRegion" set as (−3000, 3000) for annotation. The "narrowPeak" files were transformed into GrangesList forms, and the peaks were converted into consensus counts. Data normalization and differential comparison were performed using DESeq2. Regions of differential modification were identified for downstream analyses using a *p*-value cutoff of 0.05 (two-sided Wald test).

Referred SRCC patient transcriptome data analysis

We analyzed the genetic alteration data of 171 diffuse gastric carcinoma samples (including 144 diffuse-type adenocarcinomas and 27 signet ring cell carcinoma) obtained from the cBioPortal (https://www.cbioportal.org/) dataset. Subsequently, we investigated the occurrence of genetic alterations in *ARID1A*, *TP53*, and *PTEN*, encompassing various types of mutations (truncating, in-frame, missense, and splice site mutations), copy number variations (shallow deletions, deep deletions, gains, and amplifications), as well as structural variations in this dataset of individuals. Transcriptome data and corresponding clinical information of GC patients (SRCC, $n = 12$; Intestinal, $n = 74$) were obtained from The Cancer Genome Atlas Stomach Adenocarcinoma (TCGA-STAD) project. Transcriptome data of gastric cancer cell lines were acquired from the Cancer Cell Line Encyclopedia (CCLE) database (SRCC, $n = 5$; other types, $n = 14$), microarray data and corresponding Lauren classifications were acquired from GSE26899 (Diffuse-type, $n = 21$; Intestinal-type, $n = 59$).

GSEA was performed using the clusterProfiler package for the SRCC/DGC versus ITGC comparison in the TCGA-STAD cohort and for the TPA versus TP comparison in tumor organoids. For organoid RNA-seq data, mouse gene symbols were converted to human orthologs before analysis. Hallmark, C2, and C5 gene sets from MSigDB v7.1 were used. The preranked function from GSEA software was performed to clarify the overall transcriptome similarity between mouse models and tumor samples of GC patients. To define SRCC signature genes, we used the standard DESeq2 pipeline to identify genes significantly upregulated in the combined SRCC and diffuse-type gastric cancer group relative to intestinal-type gastric cancer samples from the TCGA-STAD cohort ($P < 0.05$ and log2 fold change > 1).

Data visualization

The R packages ggpubr, ggplot2, and ggpaired were used to create box plots to visualize differences in gene expression and chromatin accessibility levels. Heatmaps of differentially expressed genes were generated using the pheatmap package. GO enrichment results were presented using bar plots and dot plots created with ggplot2. DeepTools was used to visualize protein-binding and chromatin accessibility profiles. Matrix computation of protein-binding and accessibility peaks was performed using the "computeMatrix reference-point –referencePoint center -b 3000 - a 3000 - skipZeros" option.

Statistical analysis

Organoid diameter and number assays, tumor measurements, RT-qPCR, morphological statistics, and in vitro treatment were analyzed for statistical significance using two-tailed unpaired parametric Student's *t*-tests (Prism 9.0, GraphPad software). The data distribution was assumed to be normal, but this was not formally tested. Statistical test methods, sample sizes, and *p*-values are indicated in the corresponding figure legends. For the in vitro treatment experiments, all samples were randomly assigned to vehicle or treatment groups. Tumor measurements were performed blindly. The measurements of organoid shapes were analyzed blindly. For other in vivo and in vitro experiments, the researchers were not blinded while performing the experiments. No data were excluded from the study. Statistical significance on RNA-seq, ATAC-seq, and CUT&Tag data was determined using unpaired two-tailed *t*-test, Wilcoxon rank-sum test, Wald test, hypergeometric distribution, or Likelihood-ratio test. Statistical significance was defined as $p < 0.05$. All the quantification and visualization of omics data analysis were performed on R v3.6.

Reporting summary

Further information on research design is available in the Nature Portfolio Reporting Summary linked to this article.

Data availability

The RNA-seq, ATAC-seq, and CUT&Tag sequencing data generated in this study have been deposited in the Gene Expression Omnibus (GEO) database under the accession numbers GSE232288, GSE232289, GSE232291, and GSE232292. RNA-seq: https://www.ncbi.nlm.nih.gov/geo/query/acc.cgi?acc=GSE232288; https://www.ncbi.nlm.nih.gov/geo/query/acc.cgi?acc=GSE232292; ATAC-seq: https://www.ncbi.nlm.nih.gov/geo/query/acc.cgi?acc=GSE232291; CUT&Tag: https://www.ncbi.nlm.nih.gov/geo/query/acc.cgi?acc=GSE232289, Analysis code for this project is available at GitHub (https://github.com/AilingZhong/SRCC_Project) and archived at Zenodo (https://doi.org/10.5281/zenodo.19588797). All data are included in the Source Data file or available from the authors. Source data are provided with this paper. The remaining data are available within the Article, Supplementary Information or Source Data file. Source data are provided with this paper.

Code availability

The analysis codes can be found in GitHub (https://github.com/AilingZhong/SRCC_Project).

References

1. Mariette, C. et al. Consensus on the pathological definition and classification of poorly cohesive gastric carcinoma. *Gastric Cancer* **22**, 1–9 (2019).
2. Bosman, F. T., World Health Organization & International Agency for Research on Cancer. *WHO Classification of Tumours of the Digestive System*. 4th edn (International Agency for Research on Cancer, 2010).
3. Hugen, N. et al. Colorectal signet-ring cell carcinoma: benefit from adjuvant chemotherapy but a poor prognostic factor. *Int. J. Cancer* **136**, 333–339 (2015).
4. Chen, L. et al. The clinicopathological features and prognosis of signet ring cell carcinoma of the esophagus: a 10-year retrospective study in China. *PLoS ONE* **12**, e0176637 (2017).
5. Benesch, M. G. K. & Mathieson, A. Epidemiology of signet ring cell adenocarcinomas. *Cancers (Basel)* https://doi.org/10.3390/cancers12061544 (2020).
6. Guo, Y. et al. Clinicopathological features and prognostic-related risk factors of gastric signet ring cell carcinoma: a meta-analysis. *Comput. Math. Methods Med.* https://doi.org/10.1155/2022/3473445 (2022).
7. Chen, C., Wang, Z. & Qin, Y. Prognosis prediction in esophageal signet-ring-cell carcinoma: a competing risk analysis. *BMC Gastroenterol.* **23**, 178 (2023).
8. Huh, C. W. et al. Signet ring cell mixed histology may show more aggressive behavior than other histologies in early gastric cancer. https://doi.org/10.1002/jso.23261 (2012).
9. Shu, Y. et al. Prognostic significance of frequent CLDN18-ARHGAP26/6 fusion in gastric signet-ring cell cancer. *Nat. Commun.* **9**, 2447 (2018).
10. Nguyen, M. D., Plasil, B., Wen, P. & Frankel, W. L. Mucin profiles in signet-ring cell carcinoma. *Arch. Pathol. Lab Med,* **130**, 799–804 (2006).
11. Yamashiro, K., Suzuki, H. & Nagayo, T. Electron microscopic study of signet-ring cells in diffuse carcinoma of the human stomach. *Virchows Arch. A Pathol. Anat. Histol.* **374**, 275–284 (1977).
12. Terada. T. An immunohistochemical study of primary signet-ring cell carcinoma of the stomach and colorectum: II. Expression of MUC1, MUC2, MUC5AC, and MUC6 in normal mucosa and in 42 cases. *Int. J. Clin. Exp. Pathol.* **6**, 613–621 (2013).
13. Murakami, H. et al. Establishment and characterization of novel gastric signet-ring cell and non signet-ring cell poorly differentiated adenocarcinoma cell lines with low and high malignant potential. *Gastric Cancer* **16**, 74–83 (2012).

14. Zhao, W. et al. Single-cell analysis of gastric signet ring cell carcinoma reveals cytological and immune microenvironment features. *Nat. Commun.* **14**, 2985 (2023).
15. Wang, Y. et al. Multilevel proteomic analyses reveal molecular diversity between diffuse-type and intestinal-type gastric cancer. *Nat. Commun.* **14**, 835 (2023).
16. Puccini, A. et al. Molecular profiling of signet-ring-cell carcinoma (SRCC) from the stomach and colon reveals potential new therapeutic targets. *Oncogene* **41**, 3455–3460 (2022).
17. Chen, J. et al. Single-cell profiling of tumor immune microenvironment reveals immune irresponsiveness in gastric signet-ring cell carcinoma. *Gastroenterology* https://doi.org/10.1053/j.gastro.2023.03.008 (2023).
18. Cancer Genome Atlas Research, N Comprehensive molecular characterization of gastric adenocarcinoma. *Nature* **513**, 202–209 (2014).
19. Yao, F. et al. Recurrent fusion genes in gastric cancer: CLDN18-ARHGAP26 induces loss of epithelial integrity. *Cell Rep.* **12**, 272–285 (2015).
20. Humar, B. et al. E-cadherin deficiency initiates gastric signet-ring cell carcinoma in mice and man. *Cancer Res* **69**, 2050–2056 (2009).
21. Yamaguchi, K. et al. Potential therapeutic targets discovery by transcriptome analysis of an in vitro human gastric signet ring carcinoma model. *Gastric Cancer* **25**, 862–878 (2022).
22. Togasaki, K. et al. Wnt signaling shapes the histologic variation in diffuse gastric cancer. *Gastroenterology* **160**, 823–830 (2021).
23. Stange, D. E. et al. Mouse models of human gastric cancer subtypes with stomach-specific CreERT2-mediated pathway alterations. *Gastroenterology* **157**, 1599–1614 (2019).
24. Shimada, S. et al. Synergistic tumour suppressor activity of E-cadherin and p53 in a conditional mouse model for metastatic diffuse-type gastric cancer. *Gut* **61**, 344–352 (2011).
25. Wilson, B. G. & Roberts, C. W. SWI/SNF nucleosome remodellers and cancer. *Nat. Rev. Cancer* **11**, 481–492 (2011).
26. Jones, S. et al. Frequent mutations of chromatin remodeling gene ARID1A in ovarian clear cell carcinoma. *Science* **330**, 228–231 (2010).
27. Mathur, R. et al. ARID1A loss impairs enhancer-mediated gene regulation and drives colon cancer in mice. *Nat. Genet.* **49**, 296–302 (2017).
28. Sun, X. et al. Arid1a has context-dependent oncogenic and tumor suppressor functions in liver cancer. *Cancer Cell* **32**, 574–589 e576 (2017).
29. Lo, Y. H. et al. A CRISPR/Cas9-engineered ARID1A-deficient human gastric cancer organoid model reveals essential and nonessential modes of oncogenic transformation. *Cancer Discov.* **11**, 1562–1581 (2021).
30. Na, F. et al. KMT2C deficiency promotes small cell lung cancer metastasis through DNMT3A-mediated epigenetic reprogramming. *Nat. Cancer* **3**, 753–767 (2022).
31. Wang, M. et al. Acquired semi-squamatization during chemotherapy suggests differentiation as a therapeutic strategy for bladder cancer. *Cancer Cell* **40**, 1044–1059.e1048 (2022).
32. Lu, Z. et al. Dissecting the genetic and microenvironmental factors of gastric tumorigenesis in mice. *Cell Rep.* **41**, 111482 (2022).
33. Steele, N. G. et al. An organoid-based preclinical model of human gastric cancer. *Cell Mol. Gastroenterol. Hepatol.* **7**, 161–184 (2019).
34. Zhang, M. et al. EZH2 loss promotes gastric squamous cell carcinoma. *Nat. Commun.* **16**, 6032 (2025).
35. Wang, J. et al. Enhancement of E-cadherin expression and processing and driving of cancer cell metastasis by ARID1A deficiency. *Oncogene* **40**, 5468–5481 (2021).
36. Yan, H. B. et al. Reduced expression of the chromatin remodeling gene ARID1A enhances gastric cancer cell migration and invasion via downregulation of E-cadherin transcription. *Carcinogenesis* **35**, 867–876 (2014).
37. Trifaro, J. M., Rose, S. D. & Marcu, M. G. Scinderin, a Ca2+-dependent actin filament severing protein that controls cortical actin network dynamics during secretion. *Neurochem Res.* **25**, 133–144 (2000).
38. Mittal, P. & Roberts, C. W. M. The SWI/SNF complex in cancer - biology, biomarkers and therapy. *Nat. Rev. Clin. Oncol.* **17**, 435–448 (2020).
39. Michel, B. C. et al. A non-canonical SWI/SNF complex is a synthetic lethal target in cancers driven by BAF complex perturbation. *Nat. Cell Biol.* **20**, 1410–1420 (2018).
40. Remillard, D. et al. Degradation of the BAF complex factor BRD9 by heterobifunctional ligands. *Angew. Chem. Int. Ed. Engl.* **56**, 5738–5743 (2017).
41. Pan, X. et al. Identifying a confused cell identity for esophageal squamous cell carcinoma. *Signal Transduct. Target Ther.* **7**, 122 (2022).
42. O'Rourke, K. P. et al. Transplantation of engineered organoids enables rapid generation of metastatic mouse models of colorectal cancer. *Nat. Biotechnol.* **35**, 577–582 (2017).
43. Cho, H. et al. Loss of ARID1A/BAF250a expression is linked to tumor progression and adverse prognosis in cervical cancer. *Hum. Pathol.* **44**, 1365–1374 (2013).
44. Faraj, S. F. et al. ARID1A immunohistochemistry improves outcome prediction in invasive urothelial carcinoma of urinary bladder. *Hum. Pathol.* **45**, 2233–2239 (2014).
45. Rehman, H. et al. ARID1A-deficient bladder cancer is dependent on PI3K signaling and sensitive to EZH2 and PI3K inhibitors. *JCI Insight* https://doi.org/10.1172/jci.insight.155899 (2022).
46. Guo, B. et al. Arid1a mutation suppresses TGF-beta signaling and induces cholangiocarcinoma. *Cell Rep.* **40**, 111253 (2022).
47. Fukunaga, Y. et al. Loss of Arid1a and Pten in pancreatic ductal cells induces intraductal tubulopapillary neoplasm via the YAP/TAZ pathway. *Gastroenterology* **163**, 466–480.e466 (2022).
48. Jana, S. et al. Transcriptional-translational conflict is a barrier to cellular transformation and cancer progression. *Cancer Cell* https://doi.org/10.1016/j.ccell.2023.03.021 (2023).
49. Xu, G. et al. ARID1A determines luminal identity and therapeutic response in estrogen-receptor-positive breast cancer. *Nat. Genet.* **52**, 198–207 (2020).
50. Wilson, M. R. et al. ARID1A mutations promote P300-dependent endometrial invasion through super-enhancer hyperacetylation. *Cell Rep.* **33**, 108366 (2020).
51. Wilson, M. R. et al. ARID1A and PI3-kinase pathway mutations in the endometrium drive epithelial transdifferentiation and collective invasion. *Nat. Commun.* **10**, 3554 (2019).
52. Gong, M. et al. Abnormal microglial polarization induced by Arid1a deletion leads to neuronal differentiation deficits. *Cell Prolif.* **55**, e13314 (2022).
53. Zhang, S. et al. mTORC1 promotes ARID1A degradation and oncogenic chromatin remodeling in hepatocellular carcinoma. *Cancer Res.* **81**, 5652–5665 (2021).
54. Zhou, W. et al. Targeting the mevalonate pathway suppresses ARID1A-inactivated cancers by promoting pyroptosis. *Cancer Cell* **41**, 740–756.e710 (2023).
55. Xu, C. et al. Comprehensive molecular phenotyping of ARID1A-deficient gastric cancer reveals pervasive epigenomic reprogramming and therapeutic opportunities. *Gut* https://doi.org/10.1136/gutjnl-2022-328332 (2023).
56. Coughtrie, M. W., Burchell, B. & Bend, J. R. A general assay for UDPglucuronosyltransferase activity using polar amino-cyano stationary phase HPLC and UDP[U-14C]glucuronic acid. *Anal. Biochem.* **159**, 198–205 (1986).

57. Wang, Z. et al. Dual ARID1A/ARID1B loss leads to rapid carcinogenesis and disruptive redistribution of BAF complexes. *Nat. Cancer* **1**, 909–922 (2020).
58. Belk, J. A. et al. Genome-wide CRISPR screens of T cell exhaustion identify chromatin remodeling factors that limit T cell persistence. *Cancer Cell* **40**, 768–786.e767 (2022).

Acknowledgements

We thank Dr. Yuquan Wei for generous support. We thank all the CC-LY lab members and Fangfang Wang (Institute of Hematology, West China Hospital) for discussion and technical support. We thank the Core Facilities of West China Hospital and the Chengdu OrganoidMed Medical Laboratory for technical support.

Author contributions

Conceptualization, C.C.; Methodology: H.Y.L., A.L.Z., Z.H.L., M.S.Z., J.X.L., Y.J.W., X.L.C., X.Y.P., J.N.Z., J.Y.C., .L.X.Z., L.M.G., S.Y.H., X.Y.W., X.D.W., T.F.P., J.W., J.J.D., X.T.D., K.Y., K.L., X.Z.C., X.L.C., Z.F., B.H.W., L.Y.Z., W.H.Z. S.Y.Y., Y.W., L.C., Z.H.X., C.J.Z., L.Z.D.; Investigation: H.Y.L., A.L.Z., Z.H.L.; Resources: L.M.G., T.F.P., K.Y., K.L., X.Z.C., X.L.C., Z.F., L.Z., W.H.Z., S.Y.Y., Y.W., L.C., Z.H.X., C.J.Z., Y.L., F.F.N.; Writing–original draft: H.Y.L., A.L.Z., Z.H.L., J.K.H., Y.L., C.C.; Writing–review & editing: H.Y.L., A.L.Z., Z.H.L., J.Y.C., Y.Y.W., J.K.H., Y.L., C.C.; Funding acquisition: H.Y.L., B.H.W., J.X., Y.L., S.Y.Y., F.F.N., Y.L., C.C.; Supervision: F.F.N., J.K.H., Y.L., C.C.

Funding

This work was supported by the Noncommunicable Chronic Diseases-National Science and Technology Major Project (2023ZD0500500 [Y.L.]); the National Natural Science Foundation of China (T2221004 [C.C.], 82330087 [C.C.], 2024YFF0507400 [C.C.], 82130007 [Y.L.], 82170171 [C.C.], 82470188 [Y.L.], 82300186 [B.W.], 82500226 [J.X]); the Sichuan Science and Technology Program (2025NSFTD0030 [Y.L.], 2025ZNSFSC0047 [C.C.]); the Frontiers Medical Center, Tianfu Jincheng Laboratory Foundation (TFJC2023010004 [C.C.]); the Post-Doctor Research Project, West China Hospital, Sichuan University (2024HXBH179 [J.Z.], 2025HXBH025 [H.L.]); the China Postdoctoral Science Foundation (2023TQ0226 [B.W.]); the From 0 to 1 innovative research project of Sichuan University (2023SCUH0070 [Q.Z.]); Natural Science Foundation of Sichuan Province of China (2024NSFSC1696 [J.X]).

Competing interests

The authors declare no competing interests.

Additional information

Supplementary information The online version contains supplementary material available at https://doi.org/10.1038/s41467-026-73933-0.

Correspondence and requests for materials should be addressed to Feifei Na, Jiankun Hu, Yu Liu or Chong Chen.

Peer review information *Nature Communications* thanks Jason Mills and the other anonymous reviewers for their contribution to the peer review of this work. A peer review file is available.

Reprints and permissions information is available at http://www.nature.com/reprints

Publisher's note Springer Nature remains neutral with regard to jurisdictional claims in published maps and institutional affiliations.

Open Access This article is licensed under a Creative Commons Attribution-NonCommercial-NoDerivatives 4.0 International License, which permits any non-commercial use, sharing, distribution and reproduction in any medium or format, as long as you give appropriate credit to the original author(s) and the source, provide a link to the Creative Commons licence, and indicate if you modified the licensed material. You do not have permission under this licence to share adapted material derived from this article or parts of it. The images or other third party material in this article are included in the article's Creative Commons licence, unless indicated otherwise in a credit line to the material. If material is not included in the article's Creative Commons licence and your intended use is not permitted by statutory regulation or exceeds the permitted use, you will need to obtain permission directly from the copyright holder. To view a copy of this licence, visit http://creativecommons.org/licenses/by-nc-nd/4.0/.

© The Author(s) 2026